The Astrophysical Journal, 630:689–704, 2005 September 10

THREE-DIMENSIONAL NUMERICAL SIMULATIONS OF THERMAL-GRAVITATIONAL INSTABILITY IN THE PROTOGALACTIC HALO ENVIRONMENT

Chang Hyun Baek,[1,2] Hyesung Kang,[1] Jongsoo Kim,[2] and Dongsu Ryu[3]
Received 2005 March 28; accepted 2005 May 30

ABSTRACT

We study thermal-gravitational instability in simplified models of protogalactic halos using three-dimensional hydrodynamic simulations. The simulations started with isothermal density perturbations of various power spectra and followed the evolution of gas with radiative cooling down to $T = 10^4$ K, background heating, and self-gravity for up to ~20 cooling times. Then cooled and condensed clouds were identified and their physical properties were examined in detail. In our models, the cooling timescale is several times shorter than the gravitational timescale. Hence, during the early stage clouds start to form around initial density peaks as a result of thermal instability. Small clouds appear first, and they are pressure-bound. Subsequently, the clouds grow through compression by the background pressure, as well as through gravitational infall. During the late stage, cloud-cloud collisions become important, and clouds grow mostly through gravitational merging. Gravitationally bound clouds with mass $M_c \gtrsim 6 \times 10^6\ M_\odot$ are found in the late stage. They are approximately in virial equilibrium and have radii $R_c \simeq 150$–200 pc. Those clouds have gained angular momentum through tidal torque, as well as merging, so they have large angular momentum with a spin parameter $\langle \lambda_s \rangle \sim 0.3$. The clouds formed in a denser background tend to have smaller spin parameters, since self-gravity, compared to radiative cooling, is relatively less important at higher density. H_2 cooling to below $T = 10^4$ K does not drastically change the evolution and properties of clouds, since it is much less efficient than the H Lyα cooling. The slope of the initial density power spectrum affects the morphology of the cloud distribution, but the properties of individual clouds do not sensitively depend on it. We point out limitations of our study and mention briefly the implications of our results for the formation of protoglobular cluster clouds in protogalactic halos.

Subject headings: cosmology: theory — gravitation — hydrodynamics — instabilities — methods: numerical

1. INTRODUCTION

Thermal instability (TI) is one of key physical processes in astrophysical environments where optically thin gas cools radiatively and condenses (Field 1965). It has been applied to explain, for instance, the multiple phases of interstellar gas (e.g., Field et al. 1969; McKee & Ostriker 1977), the formation of globular clusters (e.g., Fall & Rees 1985), cooling flows in clusters of galaxies (e.g., Nulsen 1986), and the generation of turbulent flows in the interstellar medium (ISM; e.g., Koyama & Inutsuka 2002; Kritsuk & Norman 2002). Cold dense clumps or clouds that are confined by the background pressure can form in a hot, radiatively cooling medium via TI (see, e.g., Burkert & Lin 2000). In the simplistic picture of TI, those overdense regions undergo quasi-static compression in near pressure equilibrium (Field 1965). However, this isobaric condensation occurs only when the clouds are small enough to adjust to pressure changes faster than the gas cools. According to numerical simulations of the collapse of thermally unstable clouds (e.g., David et al. 1988; Brinkman et al. 1990; Malagoli et al. 1990; Kang et al. 2000; Baek et al. 2003), the clouds may undergo supersonic compression when the cloud size is comparable to the cooling scale, $l_{\rm cool}$ (the distance over which a sound wave travels in a cooling time), while clouds much larger than this scale cool isochorically.

It has been suggested that the TI could be responsible for the formation of protoglobular cluster clouds (PGCCs) in protogalactic halos, which can explain the origin of old halo globular clusters (e.g., Fall & Rees 1985; Kang et al. 2000). Among the many models of globular cluster formation (see, e.g., Parmentier et al. 1999; Kravtsov & Gnedin 2005), this TI-based model is classified as a secondary model. Cold dense clouds in hot background gas develop through TI in protogalactic halos, and the condensed clouds further collapse to become globular clusters. We previously studied the development of TI in detail using one- and two-dimensional numerical simulations with spherically symmetric and axisymmetric isolated gas clouds in static environments of uniform density (Kang et al. 2000; Baek et al. 2003). However, according to the current paradigm of cold dark matter models of structure formation, large protogalaxies comparable to the Milky Way formed via hierarchical clustering of smaller systems. Hence, inevitably density perturbations should exist on a wide range of length scales inside the protogalactic halos, and an ensemble of clumps should emerge. In addition, although the thermal process initiates the formation of the clumps, eventually self-gravity should become important, since the gravitational timescale is just a few times longer than the cooling timescale. As a result, the initial clumps grow by both thermal and gravitational processes to become bound clouds. Hence, thermal-gravitational instability should be considered (see, e.g., Balbus 1986).

In this paper we study thermal-gravitational instability in a hot background whose physical parameters are relevant for protogalactic halo gas. Three-dimensional simulations were made. The simulations started with random Gaussian density perturbations of various power spectra. The evolution of gas under the influence of thermal-gravitational instability was followed up to the formation of gravitationally bound clouds. The physical properties of the clouds are examined in detail. Our goal is to study how self-gravity and gravitational interactions affect the physical and dynamical properties of clouds that condense initially via TI. Although our models are as yet too simple to be applied directly to the real situation, we try to extract the implications of our

[1] Department of Earth Sciences, Pusan National University, Pusan 609-735, South Korea; chbaek@pusan.ac.kr, kang@uju.es.pusan.ac.kr.
[2] Korea Astronomy and Space Science Institute, Whaam-Dong, Yuseong-Gu, Taejeon 305-348, South Korea; jskim@kasi.re.kr.
[3] Department of Astronomy and Space Science, Chungnam National University, Daejeon 305-764, South Korea; ryu@canopus.cnu.ac.kr.

TABLE 1
Model Parameters for Simulations

Model	No. of Grid Zones	t_{end} (t_{cool})[a]	t_{end} (t_{grav})[b]	T_{min} (K)	P_k	n_h[c] (cm^{-3})
S1024	1024^3	16	2.29	10^4	Constant	0.1
S0512	512^3	20	2.86	10^4	Constant	0.1
S0256	256^3	20	2.86	10^4	Constant	0.1
K0512	512^3	20	2.86	10^4	$\propto k^{-5/3}$	0.1
R0512	512^3	20	2.86	10^4	$\propto k^2$	0.1
C0512	512^3	20	2.86	10^2	Constant	0.1
D0512	512^3	20	1.65	10^4	Constand	0.3

Note.—The simulation box size $L = 10$ kpc in all models.
[a] The value of $t_{cool} = 2 \times 10^7$ yr in the models with $n_h = 0.1$ cm^{-3} and 6.7×10^6 yr in the models with $n_h = 0.3$ cm^{-3}.
[b] The value of $t_{grav} = 1.4 \times 10^8$ yr in the models with $n_h = 0.1$ cm^{-3} and 8.1×10^7 yr in the models with $n_h = 0.3$ cm^{-3}.
[c] The value of $\rho_h = (2.34 \times 10^{-24}\text{g}) n_h$ with $n(\text{He})/n(\text{H}) = 0.1$.

results for the formation of PGCCs in protogalactic halos. In § 2 our models and numerical details are described. Simulation results are presented in § 3, followed by a summary and discussion in § 4.

2. SIMULATIONS

2.1. *Models for Protogalactic Halo*

A gas of $T_h = 1.7 \times 10^6$ K in a cubic, periodic simulation box was considered. This temperature corresponds to that of an isothermal sphere with circular velocity $V_c = 220$ km s^{-1}, representing the halo of disk galaxies like the Milky Way. The fiducial value of the mean background density of hydrogen nuclei was chosen to be $n_h = 0.1$ cm^{-3}. A case with higher density, $n_h = 0.3$ cm^{-3}, was also considered to explore the effects of background density (model D0512; see Table 1). For primordial gas with an assumed ratio of He/H number densities of 1/10, the gas mass density is given by $\rho_h = (2.34 \times 10^{-24}$ g$) n_h$. With $T_h = 1.7 \times 10^6$ K and $n_h = 0.1$ cm^{-3}, the initial cooling timescale is $t_{cool} = 2 \times 10^7$ yr. On the other hand, the free-fall, or gravitational, timescale is $t_{grav} = 1.4 \times 10^8$ yr, which is about 7 times longer than the cooling timescale. Note that $t_{cool} \propto n_h^{-1}$, while $t_{grav} \propto n_h^{-1/2}$. So cooling, compared to gravitational processes, becomes relatively more important at higher densities. The cooling length scale is given as $l_{cool} = c_h t_{cool} = 4$ kpc, where $c_h = 198$ km s^{-1} is the sound speed. The simulation box was set to have the size $L = 10$ kpc $= 2.5 l_{cool}$. It was chosen to be large enough to accommodate a fair number of thermally unstable clouds of cooling length size, and so to get fair statistics of cloud properties.

To mimic density perturbations existing on a wide range of length scales inside the protogalactic halo, the initial density field was drawn from random Gaussian fluctuations with a predefined density power spectrum. The density power spectrum was assumed to have the power law

$$P_k \equiv |\delta\rho_k|^2 4\pi k^2 \propto k^n, \tag{1}$$

where k is a three-dimensional wavenumber, $k = (k_x^2 + k_y^2 + k_z^2)^{1/2}$. In order to explore how the initial density perturbations affect the formation and evolution of clouds, three types of density power spectra were considered: white noise with $n = 0$ (the representative case), random fluctuation with $n = 2$ (model R0512), and a Kolmogorov spectrum with $n = -5/3$ (model K0512). Only the powers with values of k corresponding to wavelengths $\lambda \le L/2$ were included. The amplitude of the density power spectrum was fixed by the condition $\delta_{rms} \equiv \langle \delta\rho^2 \rangle^{1/2} / \langle \rho \rangle = 0.2$. The initial temperature was set to be uniform, assuming isothermal density perturbations. The initial velocity was set to be zero everywhere in the simulation box.

2.2. *Numerical Details*

The gasdynamical equations in a Cartesian coordinate system that includes self-gravity, radiative cooling, and heating are written as

$$\frac{\partial \rho}{\partial t} + \nabla \cdot (\rho \boldsymbol{v}) = 0, \tag{2}$$

$$\frac{\partial}{\partial t}(\rho \boldsymbol{v}) + \nabla \cdot (\rho \boldsymbol{v}\boldsymbol{v} + p\boldsymbol{I}) = -\rho \nabla \Phi, \tag{3}$$

$$\frac{\partial E}{\partial t} + \nabla \cdot [(E + p)\boldsymbol{v}] = -\rho \boldsymbol{v} \cdot \nabla \Phi + \Gamma - \Lambda, \tag{4}$$

$$\nabla^2 \Phi = 4\pi G \rho, \tag{5}$$

where $E = (1/2)\rho v^2 + p/(\gamma - 1)$, Λ and Γ are the cooling and heating rates per unit volume, and the rest of the variables have their usual meanings. For the adiabatic index, $\gamma = 5/3$ was assumed.

The hydrodynamics was solved using an Eulerian hydrodynamics code based on the total variation diminishing scheme (Ryu et al. 1993). The version parallelized with the Message Passing Interface (MPI) library was used.

The self-gravity, cooling, and heating were treated after the hydrodynamic step. For the self-gravity, the gravitational potential was calculated using the usual fast Fourier transform (FFT) technique. Then the gravitational force was implemented in a way to ensure second-order accuracy as

$$\boldsymbol{v}^{n+1} = \boldsymbol{v}^{n+1,*} - \Delta t^n \nabla \Phi^{n+1/2}, \tag{6}$$

where $\boldsymbol{v}^{n+1,*}$ is the velocity updated in the hydrodynamic step and $\Phi^{n+1/2}$ is the potential calculated with $\rho^{n+1/2} \equiv (\rho^n + \rho^{n+1})/2$.

For the radiative cooling, the collisional ionization equilibrium (CIE) cooling rate for a zero-metallicity (primordial), optically thin gas in the temperature range of 10^4 K $\le T \le 10^{7.5}$ K was adopted (Sutherland & Dopita 1993). The cooling function, $L(T) \equiv \Lambda / n_H^2$, is plotted in Figure 1 as a solid line. With $L(T) = 0$ for $T < 10^4$ K, it was assumed that the extragalactic/stellar UV radiation photodissociates H_2 molecules in the protogalactic halo and so prohibits the gas from cooling below 10^4 K.

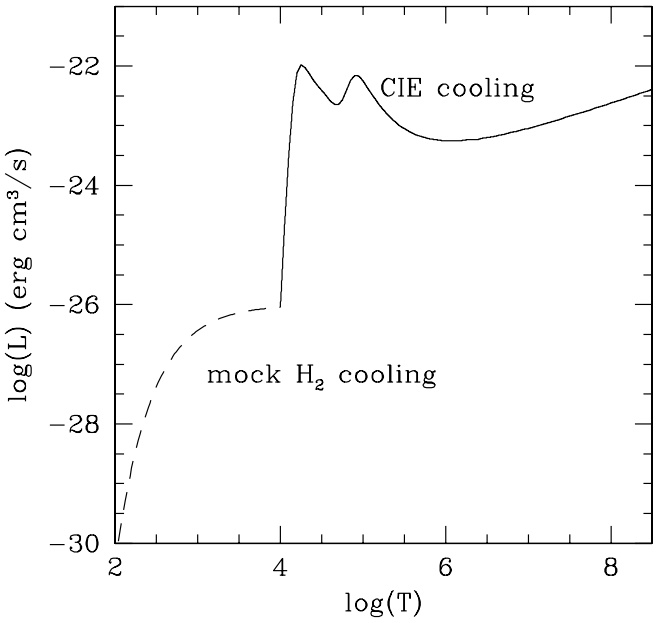

FIG. 1.—Cooling function, $L(T) \equiv \Lambda/n_{\rm H}^2$, of CIE cooling for a gas with zero metallicity (*solid line*). The dotted line is for the mock H_2 cooling adopted in model C0512.

Accordingly, the minimum temperature was set to be $T_{\rm min} = 10^4$ K. Note that the CIE cooling rate is higher than the cooling rate based on the nonequilibrium ionization, which had been adopted in our previous two-dimensional simulations, especially near the H and He Lyα line emission peaks (see Fig. 1 of Baek et al. 2003). The higher cooling rate was chosen to accentuate the effects of cooling over those of gravitational processes.

If H_2 molecules had been formed efficiently enough via gas phase reactions to be self-shielded from the photodissociating UV radiation, or if the halo gas had been enriched by metals from first-generation supernovae, however, the gas would have cooled to well below 10^4 K. In order to explore how the additional cooling below 10^4 K affects the formation and evolution of clouds in a comparison model (model C0512), the following mock cooling function in the range of 10^2 K $\leq T \leq 10^4$ K was adopted:

$$L_{\rm H_2} = 1.0 \times 10^{-26} \exp\left(-\frac{10^3}{T}\right) \ {\rm ergs\ cm^3\ s^{-1}}. \qquad (7)$$

Although this mock cooling rate was designed to represent typical H_2 rovibrational line emissions for a gas with H_2 abundance of $n_{\rm H_2}/n_{\rm H} \sim 10^{-3}$ (Shapiro & Kang 1987), the exact amplitude and form of $L_{\rm H_2}$ are not important in our discussion. Figure 1 shows $L_{\rm H_2}$ as a dashed line. The minimum temperature was set to be $T_{\rm min} = 10^2$ K in model C0512.

It was assumed that the background gas was initially under thermal balance and that there existed a constant background heating equal to the cooling of the initial background gas, that is,

$$\Gamma = L(T_h) n_h^2. \qquad (8)$$

To prevent any spurious heating, the highest temperature was set to be $T_{\rm max} = T_h$. This ad hoc heating was applied in order to maintain the temperature of the background gas with the initial mean density at $T \simeq T_h$. This can be provided by several physical processes, such as turbulence, shocks, stellar winds, and supernova explosions in protogalaxies. Without this heating the background gas would have cooled down in a few $t_{\rm cool}$.

It has been pointed out that thermal conduction can profoundly affect TI in the ISM (e.g., McKee & Begelman 1990; Koyama & Inutsuka 2004). With the Spitzer value of thermal conductivity for ionized gas, $\kappa \sim 5 \times 10^{-7} T^{5/2}$ ergs s^{-1} cm^{-1} K^{-1} (Spitzer 1979), the thermal conduction timescale is

$$t_{\rm cond} \sim 2 \times 10^9 \left(\frac{T}{1.7 \times 10^6\ {\rm K}}\right)^{-5/2} \left(\frac{n}{10^{-1}\ {\rm cm^{-3}}}\right) \left(\frac{L}{1\ {\rm kpc}}\right)^2 {\rm yr}. \qquad (9)$$

This shows that $t_{\rm cond}$ is much longer than $t_{\rm cool}$ across the cooling length ($l_{\rm cool} = 4$ kpc), so the thermal conduction is expected to be negligible. But the clouds that finally emerged in our simulations have radii of $R_c \sim 150$–200 pc (see § 3.3). Even on this scale $t_{\rm cond}$ is still a few times longer than, or at most comparable to, $t_{\rm cool}$. Also, those clouds are gravitationally bound, so the thermal evaporation should not be important. In addition, a weak magnetic field, if it exists, may significantly reduce the value of thermal conductivity from the Spitzer value (e.g., Chandran & Cowley 1998), although we do not explicitly include magnetic field in this work. All in all, it is expected that thermal conduction does not play a major role in the regime we are interested in, and hence we ignored it in our simulations.

2.3. *Model Parameters*

Simulations were made with 1024^3, 512^3, and 256^3 grid zones, allowing a uniform spatial resolution of $\Delta l = 9.8$–39 pc. Simulations started at $t = 0$ and lasted up to $t_{\rm end} = (16$–$20) t_{\rm cool}$. This terminal time corresponds to $\sim(2$–$3) t_{\rm grav}$, so gravitationally bound clouds should have emerged by then.

A total of seven simulations are presented in this paper, which differ in numerical resolution, the power spectrum of the initial density perturbations, cooling, and mean background density. Model parameters are summarized in Table 1.

3. RESULTS

3.1. *Evolution of Halo Gas*

We start to describe the results by looking at the global evolution of gas and its morphological distribution. Figure 2 shows the density power spectrum at different times in model S1024, in which $P_k \propto$ constant initially. In the figure the dimensionless wavenumber is given as $k \equiv L/\lambda$, which counts the number of waves with wavelength λ inside a simulation box of size L. The power spectrum is presented in a way that

$$\int P_k\, dk = \langle \rho^2 \rangle. \qquad (10)$$

With $t_{\rm cool} < t_{\rm grav}$, initially TI should work. The noticeable features in the early evolution of the power spectrum are the following. While $t \lesssim 2 t_{\rm cool}$ the powers with $k \gtrsim 40$ (or $\lambda \lesssim l_{\rm cool}/16$) are reduced significantly, and then the powers on those small scales grow back by $\sim 4 t_{\rm cool}$. The initial decrease of small-scale powers is a consequence of initial isothermal density perturbations. The accompanying pressure fluctuations have generated sound waves, and those sound waves have ironed out the perturbations of small scales. The follow-up, fast growth of small-scale powers is due to the nonlinear behavior of TI. Although the linear growth rate is independent of scale (for $\lambda < l_{\rm cool}$), the growth can be limited once the density increases and the cooling length becomes smaller than the perturbation scale. With the perturbation scale smaller than the cooling length, further condensation progresses isochorically and the growth slows down.

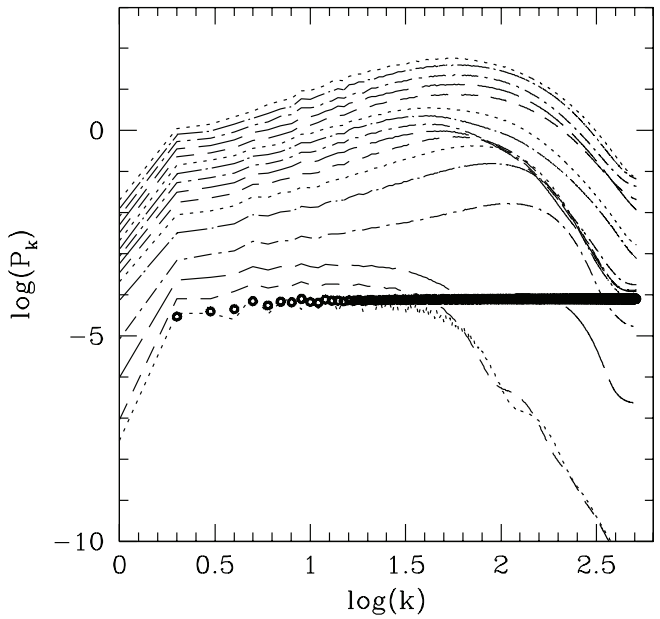

FIG. 2.—Evolution of the density power spectrum in model S1024. Circles represent the initial power spectrum at $t = 0$, and lines represent the power spectrum at $t_{\rm cool}$, $2t_{\rm cool}$, $3t_{\rm cool}$, . . . , $16t_{\rm cool}$.

As a result, small-scale clumps appear first. This point has been made previously, for example by Burkert & Lin (2000). In addition, when perturbations are compressed by background pressure, the density in the central region increases first and clouds form inside out. This contributes to the fast growth of small-scale powers too. By the end of this early TI stage, $\sim 4t_{\rm cool}$, the power spectrum peaks at $\lambda \sim l_{\rm cool}/50$.

After $\sim 4t_{\rm cool}$, self-gravity starts to play a role. Clouds grow through gravitational infall, as well as through compression by the background pressure. Eventually, massive clouds form through cloud-cloud collisions or merging among clouds (see below). During these stages, the powers grow over all scales. At the same time, the peak shifts to smaller wavenumbers, reflecting the appearance of larger, massive clouds

We note that with a periodic boundary, once the power of the scale corresponding to the box size becomes nonlinear, the large-scale clustering becomes saturated. The power spectrum in Figure 2 shows that in model S1024 the scale, which has gone nonlinear by the end, is $\sim L/2$–$L/3$, indicating that the assumption of a periodic boundary should not have affected our results significantly. In any case, our major focus is on the properties of individual clouds rather than their clustering.

In order to show how clouds form and grow, as well as how their distribution evolves, three-dimensional isodensity surfaces at four different times in model S1024 are presented in Figure 3. As noted above, at the end of the early TI stage ($\sim 4t_{\rm cool}$) mostly

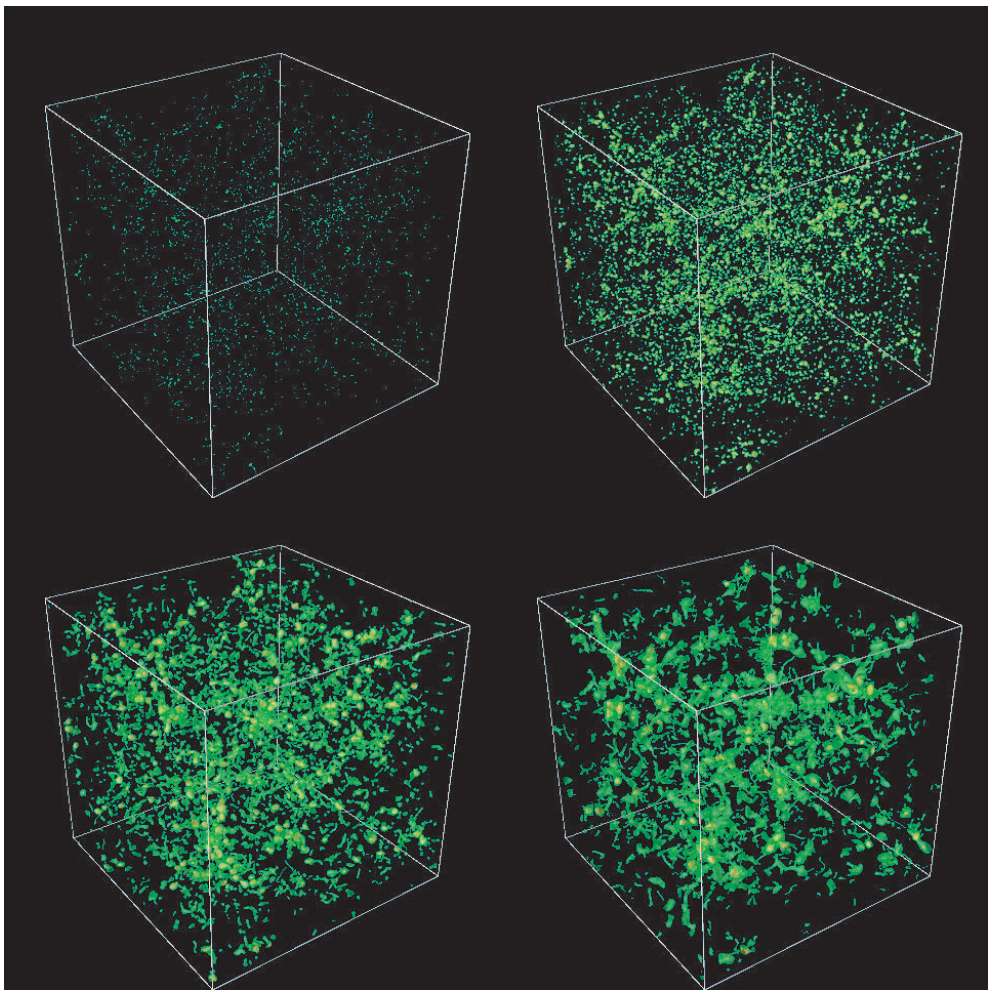

FIG. 3.—Isodensity surfaces inside the full simulation box of size 10 kpc at $4t_{\rm cool}$ (*top left*), $8t_{\rm cool}$ (*top right*), $12t_{\rm cool}$ (*bottom left*), and $16t_{\rm cool}$ (*bottom right*) in model S1024. Green surfaces correspond to $10\rho_0$, yellow surfaces to $10^2\rho_0$, and red surfaces to $10^3\rho_0$. Here ρ_0 is the mean initial density.

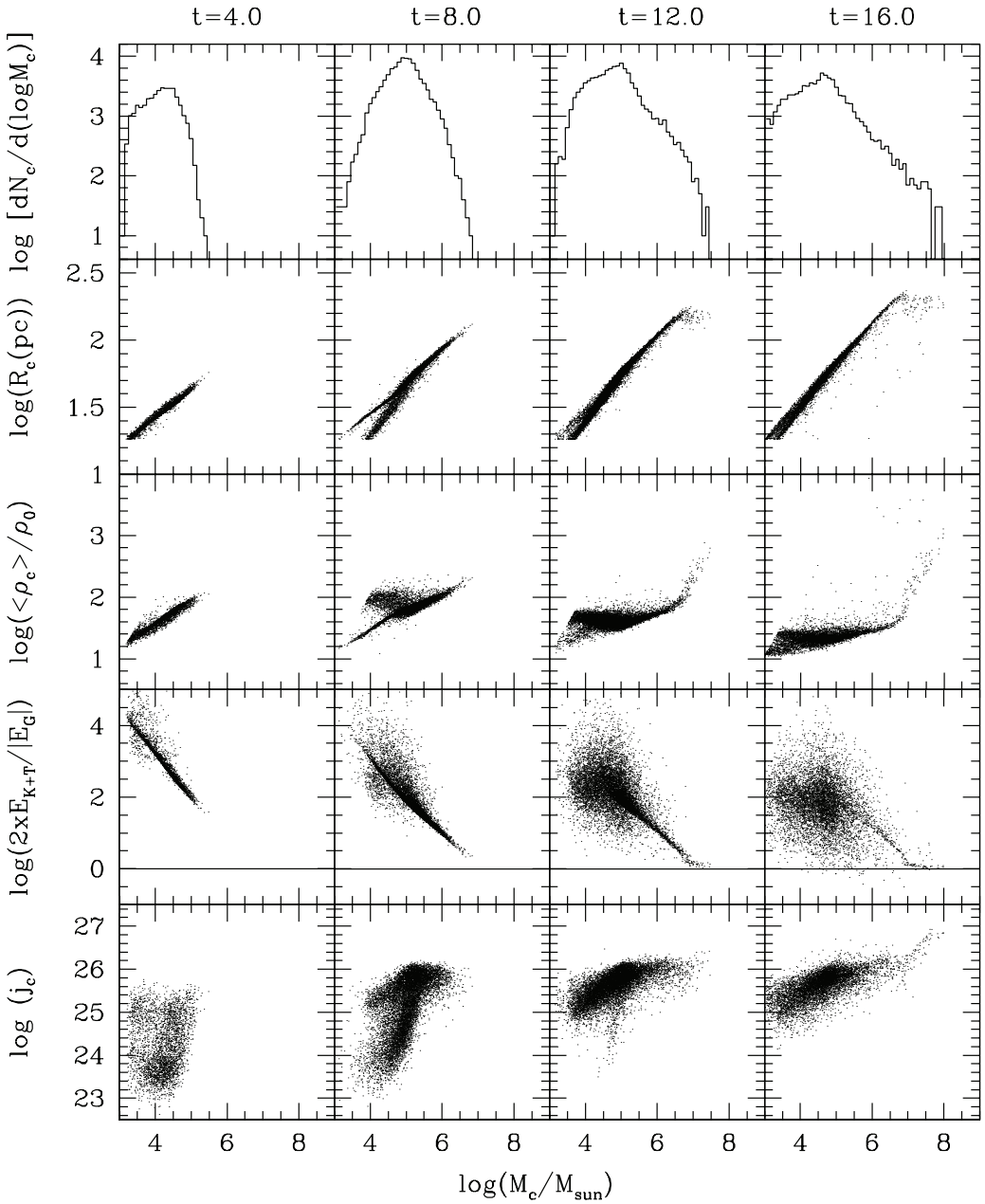

FIG. 4.—Differential number of clouds $dN_c/d(\log M_c)$, effective radius R_c, mean density $\langle\rho\rangle_2$, energy ratio $2(E_T + E_K)/|E_G|$, and specific angular momentum j_c, as a function of cloud mass, M_c, at four different times in model S1024. Here j_c is in cgs units.

small clouds appear. By the end of the follow-up stage of TI and gravitational growth, $\sim 8t_{\rm cool}$, the clouds become larger. During the late stage, the clouds become even larger, but their number decreases as a result of cloud-cloud mergers, which can be seen in the bottom two images.

3.2. *Identification of Clouds and Their Mass Function*

In order to study the properties of formed clouds, they were identified using the algorithm `clumpfind`, described by Williams et al. (1994). The algorithm basically tags cells around a density peak as "cloud cells" if they satisfy the prescribed criteria of density and temperature. We chose the following criteria: $\rho \geq 10\rho_0$ and $T \leq 10^5$ K. Here ρ_0 is the initial mean density. There is an arbitrariness in these threshold values, but the identification of clouds does not depend sensitively on the choice of threshold value, since clouds are well delineated by rather sharp jumps in density and temperature. In addition, we qualified only those with at least $3 \times 3 \times 3$ cells as clouds. Once clouds were identified, their various quantities were calculated.

The first row of Figure 4 shows the number of clouds, N_c, as a function of the cloud mass, M_c, at the same times as those in Figure 3 in model S1024. By $4t_{\rm cool}$ a significant number of clouds, $N_c \sim 3 \times 10^3$, forms through the growth of initial high-density peaks by TI. The mass function at $4t_{\rm cool}$ is roughly Gaussian, since the initial density perturbations were drawn from a random Gaussian distribution. During the follow-up stage of TI and gravitational growth, more peaks develop into clouds and at the same time become massive. The mass function evolves roughly into a lognormal distribution, shown at $8t_{\rm cool}$. The lognormal distribution is a signature of nonlinear structure formation, as reported in various simulations (see, e.g., Vázquez-Semadeni 1994; Wada & Norman 2001). During the late stage, more massive clouds develop through gravitational merging as indicated in Figure 3, and so the mass function extends to higher mass. The high-mass tail

of the mass function beyond the peak follows approximately a power-law distribution. When the mass function is fitted to $dN/dM_c \propto M_c^{-\alpha}$ for $M_c > 10^{5.5}\ M_\odot$, the value of α decreases from $\sim$0.8 at $12t_{\rm cool}$ to $\sim$0.6 at $16t_{\rm cool}$.

3.3. *Size, Density, and Energetics of Clouds*

With the mass, M_c, and volume, V_c, of identified clouds, the effective radius was taken as $R_c \equiv (3V_c/4\pi)^{1/3}$ and the mean density was calculated as $\langle\rho_c\rangle = M_c/V_c$. The second and third rows of Figure 4 show R_c and $\langle\rho_c\rangle$ in model S1024. For energetics the kinetic energy relative to the cloud's center of mass E_K, the thermal energy E_T, and the gravitational energy E_G were calculated for identified clouds. The procedure by which the gravitational energy was calculated is presented in the Appendix, along with a note of caution. The fourth row of Figure 4 shows the ratio of positive to negative energies, or the virial parameter,

$$\beta \equiv \frac{2(E_K + E_T)}{|E_G|}. \tag{11}$$

The parameter β tells us whether clouds are primarily pressure-bound ($\beta \gtrsim 2$) or gravitationally bound ($\beta \lesssim 2$). Among the gravitationally bound clouds, the condition $\beta \sim 1$ indicates that they are approximately in virial equilibrium, although, strictly speaking, the condition applies only for a stable system in which the external pressure is negligible and the moment of inertia does not change with time.

During the early stage of TI ($\lesssim 4t_{\rm cool}$), as small clumps grow isobarically, their density increases gradually, but $\langle\rho_c\rangle/\rho_0$ has not yet reached the isobaric factor of $\sim(T_h/T_{\rm min}) \simeq 100$. The self-gravity is negligible, with $\beta \gg 2$ during this stage. In the follow-up stage of TI and gravitational growth ($\lesssim 8t_{\rm cool}$), pressure-bound clouds develop fully. Those clouds have roughly $\langle\rho_c\rangle/\rho_0 \sim 100$, the maximum isobaric increase from the initial density, and the mean density is a bit higher in clouds with larger mass. Their radius scales roughly as $R_c \sim M_c^{0.3}$, which can be seen in the second row of Figure 4. The virial parameter has $\beta > 2$ for all clouds, confirming that they are still gravitationally unbound. The pressure-bound clouds follow $\beta \propto M_c^{-1}$, which can be understood as follows. In those clouds, the thermal energy is dominant over the kinetic energy, i.e., $E_T \sim$ a few $\times E_K$. With $T \sim T_{\rm min}$ in those clouds, the thermal energy scales as $E_T \propto M_c$. On the other hand, the gravitational energy scales approximately as $E_G \propto M_c^2$, since larger clouds have a slightly more concentrated mass distribution.

As clouds grow further, primarily through merging in the late stage, some of them become massive enough to be gravitationally bound. After that point clouds can be divided into two populations with distinct properties (see the last two times given in Fig. 4): pressure-bound clouds with smaller mass, and gravitationally bound clouds with larger mass. The pressure-bound clouds have properties similar to those found in the earlier stage. They have mean density $\langle\rho_c\rangle \sim 100\langle\rho_{\rm bg}\rangle$, where $\langle\rho_{\rm bg}\rangle$ is the mean background density. Note that the background density continues to decrease as more mass goes into the clouds. By the end of the S1024 simulation, $16t_{\rm cool}$, only $\sim\frac{1}{4}$ of the gas mass remains in the background. So the mean density of the pressure-bound clouds decreases with time. Those pressure-bound clouds have $\beta > 2$ and follow $\beta \propto M_c^{-1}$. The gravitationally bound clouds appear first at $\sim 9t_{\rm cool}$ or $\sim 1.3t_{\rm grav}$ in model S1024. In those clouds self-gravity enhances the density, and the mean density of the clouds reaches $10^4\langle\rho_{\rm bg}\rangle$ or even higher by $16t_{\rm cool}$. The fourth row of Figure 4 shows that the gravitationally bound clouds are approximately in virial equilibrium, with $\beta \sim 1$. In addition, we found that in those clouds the kinetic energy is not smaller but sometimes larger than the thermal energy, as expected in a virialized system, and both the gravitational energy, E_G, and the positive energy, $E_K + E_T$, scale as M_c^2.

Two points are noted regarding the gravitationally bound clouds: (1) Although these clouds have $\beta \sim 1$, they are not in steady state. The clouds lose positive energy rather quickly through cooling and contract further. But at the same time the cloud mass continues to grow through merging. (2) The gravitational energy of these gravitationally bound clouds scales as $E_G \propto M_c^2$, because their radius is in a relatively narrow range of 150–200 pc regardless of their mass, as shown in the second row of Figure 4. Since there is no physically obvious reason why clouds with different mass should have similar radii, this should be understood as the result of dynamical evolution. However, their radius is somewhat larger at $16t_{\rm cool}$ than at $12t_{\rm cool}$. This is related to the increase of angular momentum in the clouds with time (see the next subsection).

The distinction between the pressure-bound and gravitationally bound clouds in the late stage can be understood with the critical mass

$$M_{\rm crit} = 1.18\left(\frac{kT_c}{\mu m_{\rm H}}\right)^2 G^{-3/2} p_{\rm bg}^{-1/2}, \tag{12}$$

which is the maximum stable mass for an isothermal sphere confined by the background pressure $p_{\rm bg}$ (see, e.g., McCrea 1957; Kang et al. 2000). For $T_c = 10^4$ K and background pressure 4 times smaller than the initial pressure (due to decrease in the background density), the critical mass is $M_{\rm crit} \simeq 6\times10^6\ M_\odot$, which coincides well with the transition mass scale in the last two times given in Figure 4. Incidentally, this mass is similar to the Jeans mass of clouds, which is given as

$$M_{\rm J} \equiv \rho\lambda_{\rm J}^3 = 6\times10^6\left(\frac{T_c}{10^4\ {\rm K}}\right)^{3/2}\left(\frac{n_c}{100\ {\rm cm^{-3}}}\right)^{-1/2}, \tag{13}$$

where $\lambda_{\rm J}$ is the Jeans length (see, e.g., Spitzer 1979).

Although the simulated model would be too simple to represent a real protogalactic halo, it is tempting to regard the gravitationally bound clouds as possible candidates for PGCCs. That is, some of them may cool down further, to below 10^4 K, either by UV self-shielding of H_2 molecules or by self-enrichment of metals due to first-generation Type II supernovae, possibly leading to star formation. If about 10 of them turn into globular clusters, their number density would be $\sim$0.01 clusters kpc^{-3}. However, the typical size of globular clusters is $\sim$10 pc or so. So the clouds should contract further by more than a factor of 10. But the further collapse is controlled by the rotation of clouds (see § 3.4 below). In addition, the typical mass of globular clusters is $\sim 10^6\ M_\odot$ or so. So if these gravitationally bound clouds were to become globular clusters, the star formation efficiency should be $\sim$10% or so, with $\sim$90% of their mass dispersed back to protogalactic halo.

It was pointed out by Truelove et al. (1997) that "artificial fragmentation" due to errors arising from discretization occurs in numerical simulations with self-gravity. They argued that the artificial fragmentation can be suppressed if resolution is maintained high enough that, for instance, the "Jeans number" $\Delta l/\lambda_{\rm J} \lesssim 0.25$ or so for isothermal collapses. Here $\lambda_{\rm J}$ is the local Jeans length. We found that although the constraint was not complied with in a few high-density zones, $\Delta l/\lambda_{\rm J}$ was always kept smaller than 0.4 in the S1024 simulation. In any case, we followed

the evolution only up to the formation of bound clouds, not the subsequent evolution leading to the fragmentation of those clouds. So no obvious fragmentation was observed.

3.4. *Rotation of Clouds*

An important property of clouds that controls the dynamical state and affects the eventual fate is their rotation. To quantify it, the angular momentum of clouds relative to their center of mass, J_c, was calculated. The bottom row of Figure 4 shows the specific angular momentum of clouds, $j_c = J_c/M_c$, in model S1024.

In pressure-bound clouds, rotation plays a minor role in their dynamical evolution, since the rotational energy is smaller by an order of magnitude than the thermal energy. But we found that rotation can be dynamically important in gravitationally bound clouds. The specific angular momentum of those gravitationally bound clouds is larger than that of pressure-bound clouds, which can be seen clearly at $16t_{\rm cool}$. In fact, gravitationally bound clouds with the same M_c have higher angular momentum at a later time. For example, for clouds with $M_c \sim 10^{7.5}\ M_\odot$, j_c is a few times larger at $16t_{\rm cool}$ than at $12t_{\rm cool}$. This is because the clouds have grown mostly through merging in the late stage and have gained angular momentum through merging, as well as tidal torque. The direct consequence is that the clouds at later stages have a larger radius, as noted in § 3.3. We note that the clouds in our simulations are ever evolving. So it is not meaningful to define the canonical properties of clouds such as R_c and j_c as functions of M_c.

The rotation of gravitationally bound objects is often characterized by the dimensionless spin parameter (Peebles 1969)

$$\lambda_s = \frac{J_c |E_G^{1/2}|}{G M_c^{5/2}}. \tag{14}$$

This measures the degree of rotational support of the systems with

$$\frac{f_{\rm centrifugal}}{f_{\rm gravity}} \sim \frac{J_c}{{R_c}^3} \frac{R_c^2}{GM_c} \sim \lambda_s^2. \tag{15}$$

In the context of cosmological N-body simulations, it has been shown that the typical value of λ_s for gravitationally bound objects that acquired angular momentum through gravitational torque is ~0.05 (see, e.g., Barnes & Efstathiou 1987). In Figure 5 red squares represent the spin parameter for the gravitationally bound clouds with $M_c \geq 10^7\ M_\odot$ at $16t_{\rm cool}$ in model S1024. It is clear that λ_s of our gravitationally bound clouds is significantly larger than 0.05. All except one have $\lambda_s > 0.05$, and the mean value is $\langle \lambda_s \rangle \sim 0.3$. This is because the clouds have gained angular momentum through merging as well as torque.

With such large values of λ_s, the degree of rotational support of the gravitationally bound clouds should be already substantial. Hence, rotation is the key parameter that determines whether some of those clouds could become PGCCs and then collapse further to become globular clusters. For instance, in a dissipative collapse that conserves angular momentum, the clouds with $\lambda_s \sim 0.3$ can contract only by a factor of a few before they become completely rotationally supported and disk-shaped. However, it is not yet clear whether we should conclude that those clouds with $\lambda_s \sim 0.3$ cannot evolve into globular clusters. This is because we cannot rule out the possibility that the clouds may be able to lose most, say ~99%, of their angular momentum while they collapse and lose ~90% of their mass. For instance, in the so-called self-enrichment model of globular cluster formation, first-generation Type II supernovae govern star formation and the removal of residual gas (see, e.g., Parmentier et al. 1999; Shustov & Wiebe 2000). In this model the star formation may have occurred preferentially at the core, and most of the gas in the outer area with large angular momentum may have been blown out.

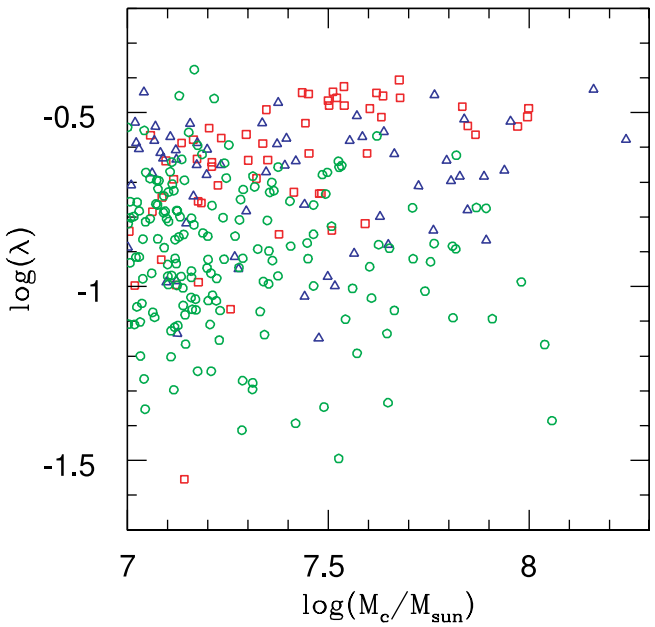

FIG. 5.—Spin parameter $\lambda_s = J|E_G^{1/2}|/GM^{5/2}$ as a function of cloud mass, M_c, for clouds with $M_c \geq 10^7\ M_\odot$. Red squares are for model S1024, blue triangles are for model S0512, and green circles are for model D0512 at $16t_{\rm cool}$.

In addition, as noted above, the gravitationally bound clouds found at an earlier time have smaller angular momentum. So if the clouds were detached from the background and started to collapse earlier, the angular momentum restriction would be somewhat less severe. Also, the clouds that emerged from different environments could have smaller angular momentum (for instance, see § 3.8). In any case, the subsequent evolution of the gravitationally bound clouds is beyond the scope of this paper, so we leave the possible connection between these clouds and PGCCs to future study.

3.5. *Shape of Clouds*

Shape is another property of clouds that reflects their dynamical state. In order to quantify it, we examined the shape parameters, defined as

$$q \equiv \frac{b}{a}, \quad s \equiv \frac{c}{a}, \tag{16}$$

with each cloud fitted to a triaxial ellipsoid with axes of $a \geq b \geq c$. The shape parameters have been commonly used to study clumps in numerical simulations (e.g., Curir et al. 1993; Gammie & Lin 2003). In order to find them, first the moment of the inertia tensor,

$$I_{ij} = \int \rho x_i x_j d^3\boldsymbol{x}, \tag{17}$$

was constructed for each cloud. Here $\boldsymbol{x}$ is the displacement relative to the cloud's center of mass and the integral is taken

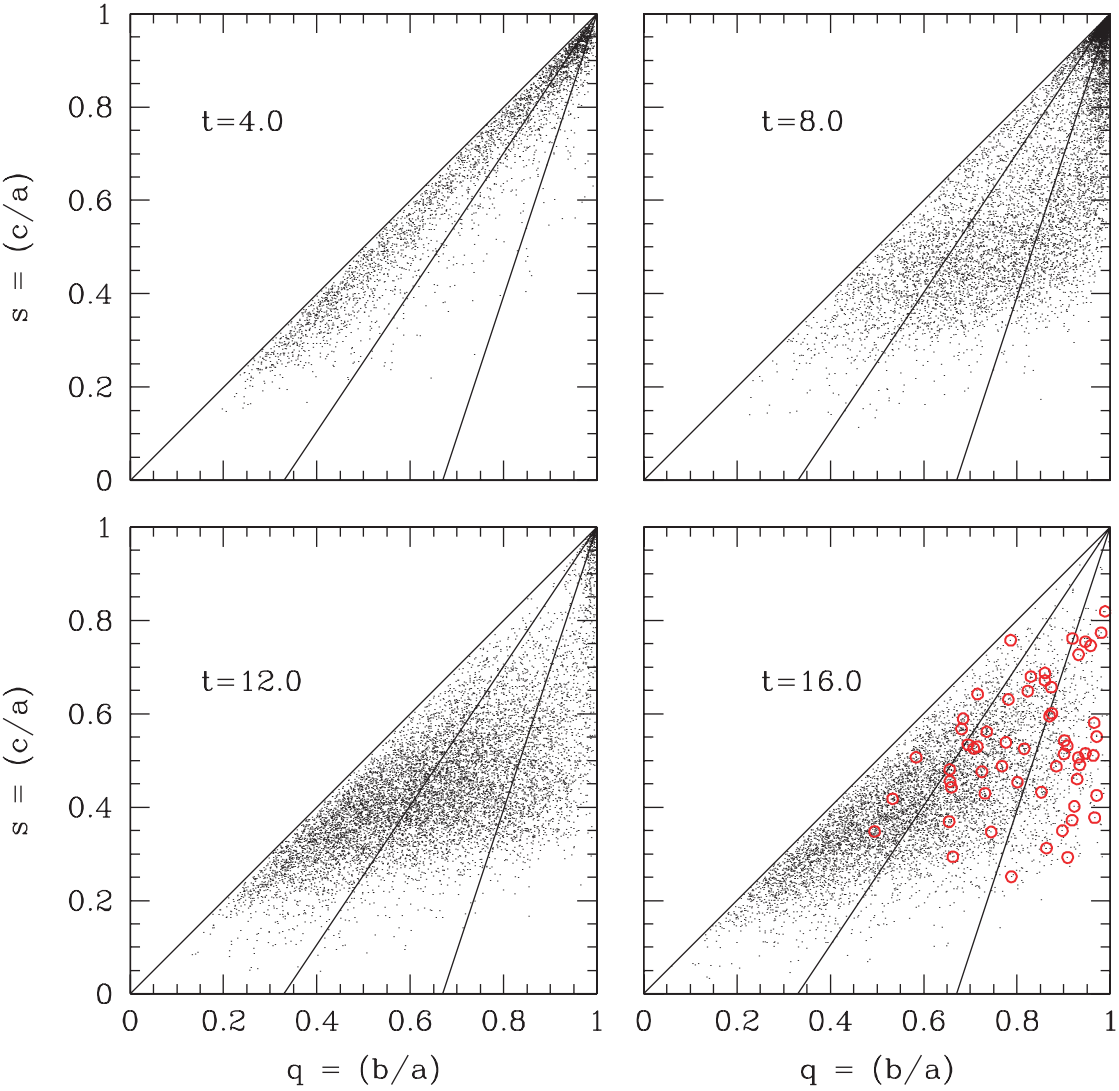

FIG. 6.—Shape parameters $q = b/a$ and $s = c/a$ at four different times in model S1024. The principal axes of clouds are defined such that $a \geq b \geq c$. The domain is divided into three regions containing clouds of prolate shape ($s \sim q < 1$; *left*), oblate shape ($s < 1$ and $q \sim 1$; *right*), and triaxial shape ($s < q < 1$; *middle*). Red circles represent clouds with $M_c \geq 10^7\ M_\odot$.

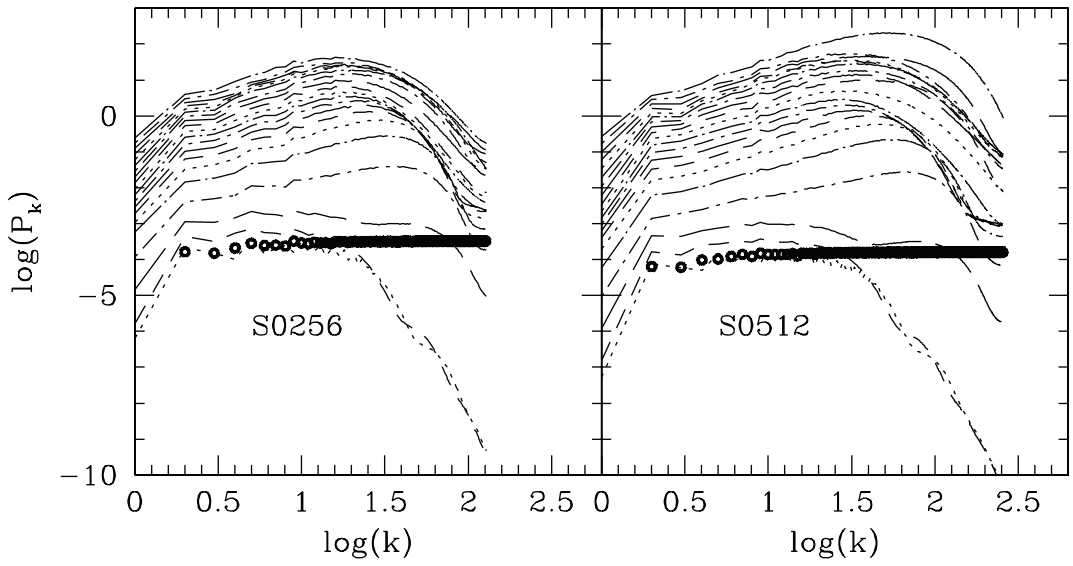

FIG. 7.—Evolution of the density power spectrum in the models S0256 and S0512. Circles represent the initial power spectrum at $t = 0$ and lines show the power spectrum at $t_{\rm cool}$, $2t_{\rm cool}$, $3t_{\rm cool}$, . . . , $20t_{\rm cool}$.

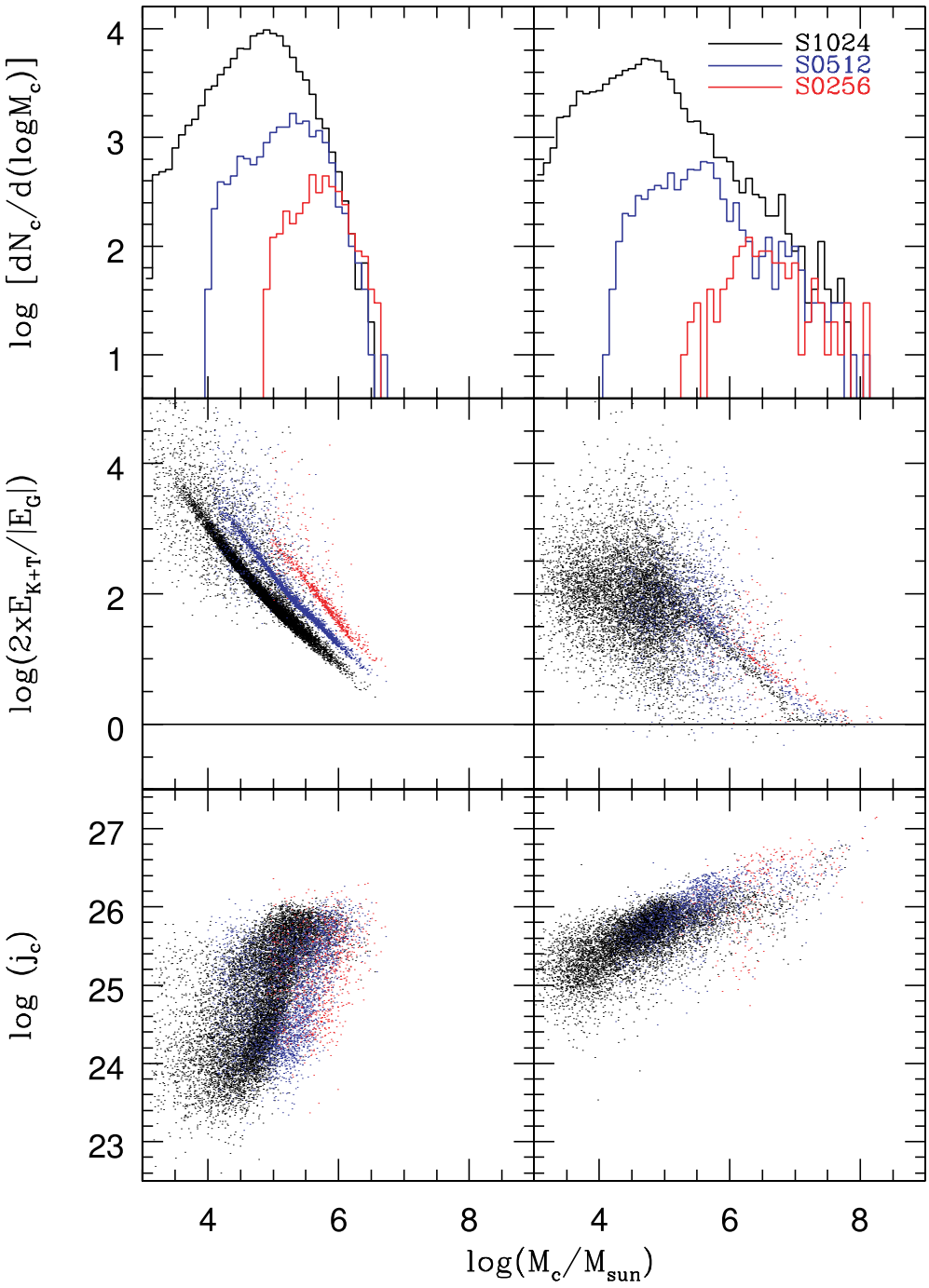

FIG. 8.—Differential number of clouds $dN_c/d(\log M_c)$, energy ratio $2(E_T + E_K)/|E_G|$, and specific angular momentum j_c as a function of cloud mass, M_c, in the three models with different resolution. The left panels show the quantities at $5t_{\rm cool}$, $6t_{\rm cool}$, and $7t_{\rm cool}$ for models S0256, S0512, and S1024, respectively. The right panels show the quantities at $15t_{\rm cool}$ for all three models. Here j_c is in cgs units.

over the cloud volume. Then, from the three eigenvalues of the tensor, $I_{11} \geq I_{22} \geq I_{33}$, the shape parameters were calculated as

$$q = \left(\frac{I_{22}}{I_{11}}\right)^{1/2}, \quad s = \left(\frac{I_{33}}{I_{11}}\right)^{1/2}. \tag{18}$$

Clouds with $s \sim q < 1$ are of prolate shape, clouds with $s < 1$ and $q \sim 1$ are of oblate shape, and clouds with $s < q < 1$ are triaxial. Spherical clouds have $s \sim q \sim 1$.

In a previous study of isolated, thermally unstable clouds using two-dimensional simulations in cylindrical geometry, we showed that the cloud shape changes in the course of the evolution (Baek et al. 2003). The degree of oblateness or prolateness is enhanced during the initial cooling phase, as expected. But it can be reversed later due to supersonic infall along the direction perpendicular to the initial flatness or elongation.

In Figure 6 dots represent clouds in the q-s plane at four times in model S1024. Lines divide the domain into three regions of roughly prolate (*left*), triaxial (*middle*), and oblate (*right*) shapes. The panel for $4t_{\rm cool}$ indicates that clouds formed as a result of TI at the early stage are preferentially of prolate shape. This is can be understood from the fact that filaments are the dominant morphology next to knots of clouds. By $8t_{\rm cool}$ some of prolate clouds

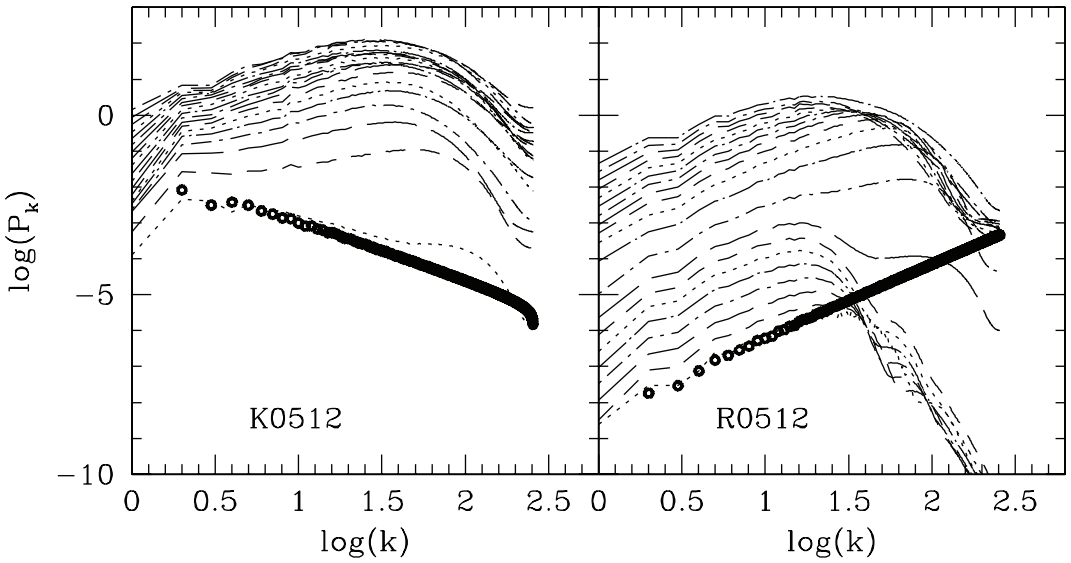

FIG. 9.—Evolution of the density power spectrum in models K0512 and R0512. Circles represent the initial power spectrum at $t = 0$, and lines represent the power spectrum at $t_{\rm cool}$, $2t_{\rm cool}$, $3t_{\rm cool}$, . . . , $20t_{\rm cool}$.

have become oblate, as the result of the shape reversal, which was observed in the two-dimensional study. However, the figure shows that in the late stage clouds tend to become prolate again. This is because gravitational merging results preferentially in clouds of an elongated prolate shape.

The gravitationally bound clouds with $M_c \geq 10^7\ M_\odot$, shown in Figure 5, are marked with red circles in the panel for $16t_{\rm cool}$. It is interesting to note that unlike most clouds, these massive clouds are preferentially of oblate shape. This is because they have large angular momentum and a substantial degree of rotational support.

3.6. *Numerical Convergence*

Convergence is an important issue in any numerical simulation. We tested it by comparing the results of simulations with different resolution, i.e., models S1024, S0512, and S0256 (see Table 1). Figure 7 shows the density power spectra of models S0512 and S0256, which can be compared with that of model S1024 in Figure 2. Note that in our simulations the amplitude of the initial power spectrum was set by the condition

$$\int_{\rm all} P_k\, dk \equiv A \int_{\rm all} k^n\, dk = \left(1 + \delta_{\rm rms}^2\right)\langle\rho\rangle^2 \qquad (19)$$

with $\delta_{\rm rms} = 0.2$ for all resolutions. Simulations with different resolution cover different ranges of wavenumbers. So the simulations of lower resolution started with larger amplitude, as shown in the figure. Otherwise, the evolution of the power spectrum looks similar in all three models. For instance, the two most noticeable features in Figure 2, i.e., the initial decrease and follow-up fast growth of small-scale powers, are also present in Figure 7. But an interesting point is that the scale that suffered the initial decrease is insensitive to resolution, because it was caused by smoothing due traveling sound waves. On the other hand, the scale of the peak in the power spectrum after the follow-up fast growth does depend on resolution. As a matter of fact, the peak at $4t_{\rm cool}$ in model S0256 occurs at a scale almost 4 times larger than in model S1024. This indicates that the small-scale growth in our simulations was limited by resolution, as expected.

Figure 8 shows the mass function, virial parameter, and specific angular momentum of clouds in the three models. The left panels show the results at the early TI stage, while the right panels show the results at the late merging stage. For the early stage a different time was chosen for each model so that the density power spectra have a similar amplitude. In the late stage, however, the differences caused by the initial amplitude of the power spectrum become insignificant, so $15t_{\rm cool}$ is chosen for all three models. We see that the mass function has converged for massive clouds, i.e., those with $M_c \gtrsim 10^6\ M_\odot$ at the early stage and those with $M_c \gtrsim 10^7\ M_\odot$ at $15t_{\rm cool}$. However, the number of smaller mass clouds depends on numerical resolution, as expected. With the minimum number of 3^3 zones for identified clouds, the minimum mass scales $M_{\rm min} \propto (\Delta l)^3$. On the the other hand, at the early stage the virial parameter is larger in lower resolutions for clouds of all mass. This is because the clouds are less compact in lower resolution, and so their gravitational energy is smaller. But as the clouds grow more massive and larger in the late stage, the difference in the virial parameter becomes smaller. The angular momentum of clouds is somewhat smaller in lower resolution at the early stage. This is partly because the time of the plot is different in different models. However, in the late stage the angular momentum becomes comparable in all three models.

Overall, the formation of small mass clouds, initially through TI and subsequently by compression and infall, was affected by resolution in our simulations. However, we found that the massive, gravitationally bound clouds, which have formed mostly through gravitational merging, have properties that almost converge.

3.7. *Effects of Initial Power Spectrum*

The effects of different initial perturbations on the formation and evolution of clouds were examined by comparing the results of simulations with different initial density power spectra, i.e., models K0512 and R0512, to those of model S0512 (see Table 1). Model K0512 started with more power on larger scales, while model R0512 started with more power on smaller scales. Figure 9 shows the density power spectra of models K0512 and R0512. In both models, small-scale powers suffered the initial decrease, as in model S0512. In particular, most of the powers

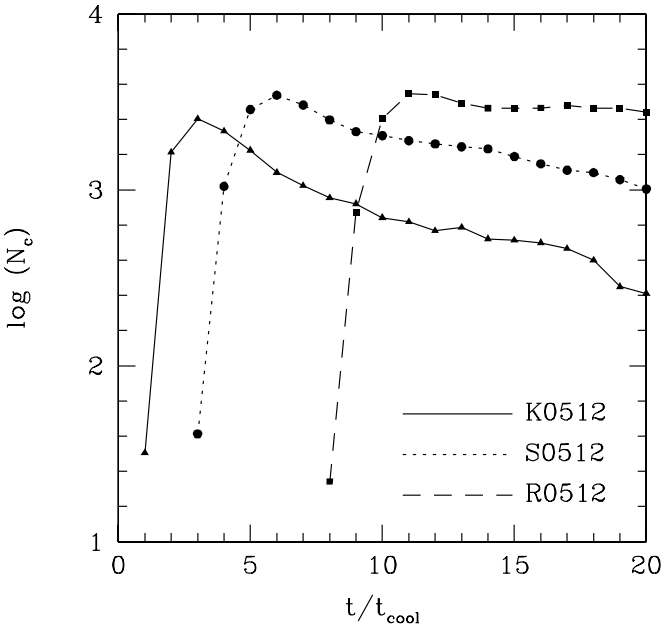

FIG. 10.—Time evolution of the number of clouds, N_c, in the three models with different initial density power spectra.

in $k \gtrsim 40$ were erased substantially in model R0512. Hence, the overall growth was delayed in model R0512. On the other hand, the growth proceeded faster in model K0512, with more powers on large scales in the beginning.

Figure 10 shows the total number of clouds as a function of time in the three models with different initial density power spectra. The overall evolution is similar; the number of clouds increases during the TI and follow-up growth stages but eventually decreases as gravitational merging progresses. As noted above, however, model K0512 evolves first and models S0512 and R0512 follow. So clouds form from $t \sim 2t_{\rm cool}$ in K0512, from $t \sim 5t_{\rm cool}$ in S0512, and from $t \sim 10t_{\rm cool}$ in R0512. However, an interesting point is that the maximum number of clouds is about the same, with $N_{\rm max} \sim 3000$ in all three models.

In Figure 11 three-dimensional isodensity surfaces are plotted at two sets of times in the three models. Different times were chosen in different models, since the formation and evolution of clouds proceeds differently. The upper panels show the surfaces when the number of clouds is highest, i.e., at $3t_{\rm cool}$ for K0512, $6t_{\rm cool}$ for S0512, and $11t_{\rm cool}$ for R0512. The lower panels show the surfaces after the number of clouds has decreased a little bit due to merging, i.e., at $4t_{\rm cool}$ for K0512, at $10t_{\rm cool}$ for S0512, and at $19t_{\rm cool}$ for R0512. The most noticeable feature is that the distribution is more "filamentary" in model K0512, but less "filamentary" in model R0512, than in model S0512. This is because that the initial large-scale powers, which were largest in model K0512 but almost absent in model R0512, have been developed into significant coherent structures in the cloud distribution.

Figure 12 shows the mass function, virial parameter, and specific angular momentum of clouds in the three models. The same two sets of times as those in Figure 11 were chosen. Clouds in the K0512 (R0512) model are slightly more (less) massive in the left panels and slightly less (more) massive in the right panels. However, considering the difference in the plotted time, the cloud mass function should be regarded as reasonably similar in the three models. On the other hand, the virial parameter of pressure-bound clouds follows the same diagonal strip in all three models. There is a spread in the distribution of angular momentum, again

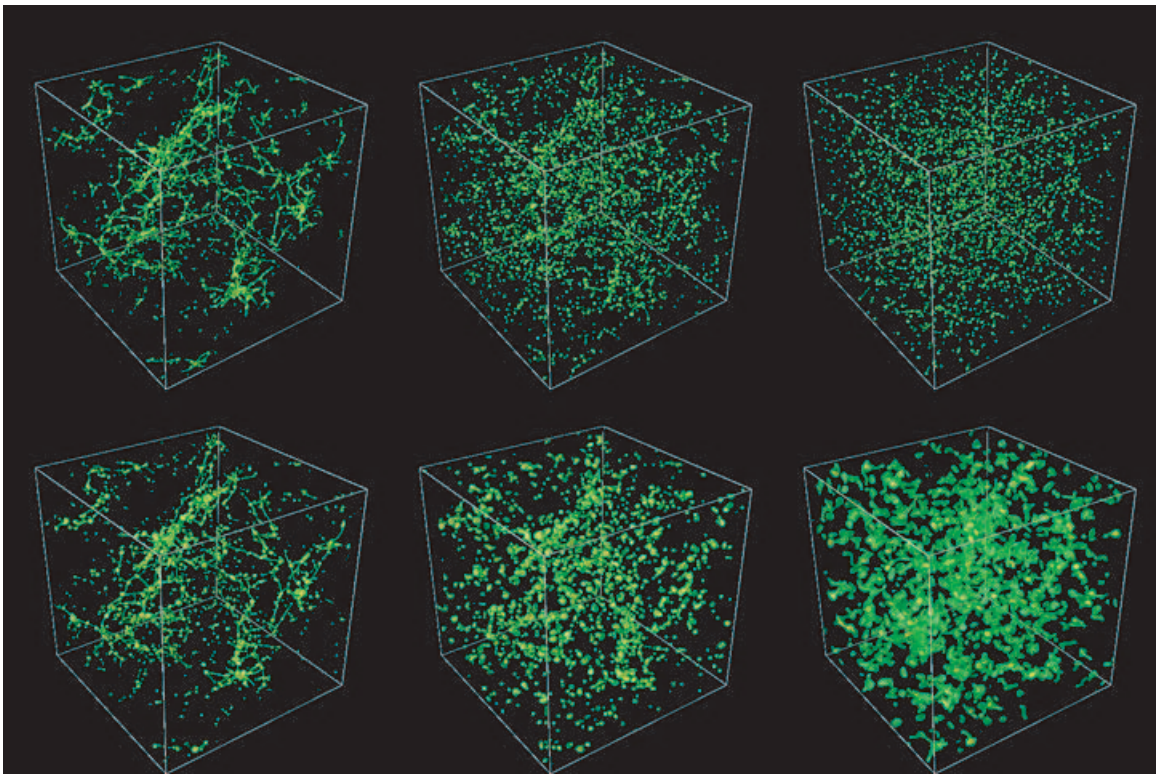

FIG. 11.—Isodensity surfaces inside the full simulation box of size 10 kpc in model K0512 (*left images*), in model S0512 (*middle images*), and in model R0512 (*right images*). The top images are at $3t_{\rm cool}$ in model K0512, at $6t_{\rm cool}$ in model S0512, and at $11t_{\rm cool}$ in model R0512. The bottom images are at $4t_{\rm cool}$ in model K0512, at $10t_{\rm cool}$ in model S0512, and at $19t_{\rm cool}$ in model R0512. Green surfaces correspond to $10\rho_0$, yellow surfaces to $10^2\rho_0$, and red surfaces to $10^3\rho_0$, as in Fig. 3.

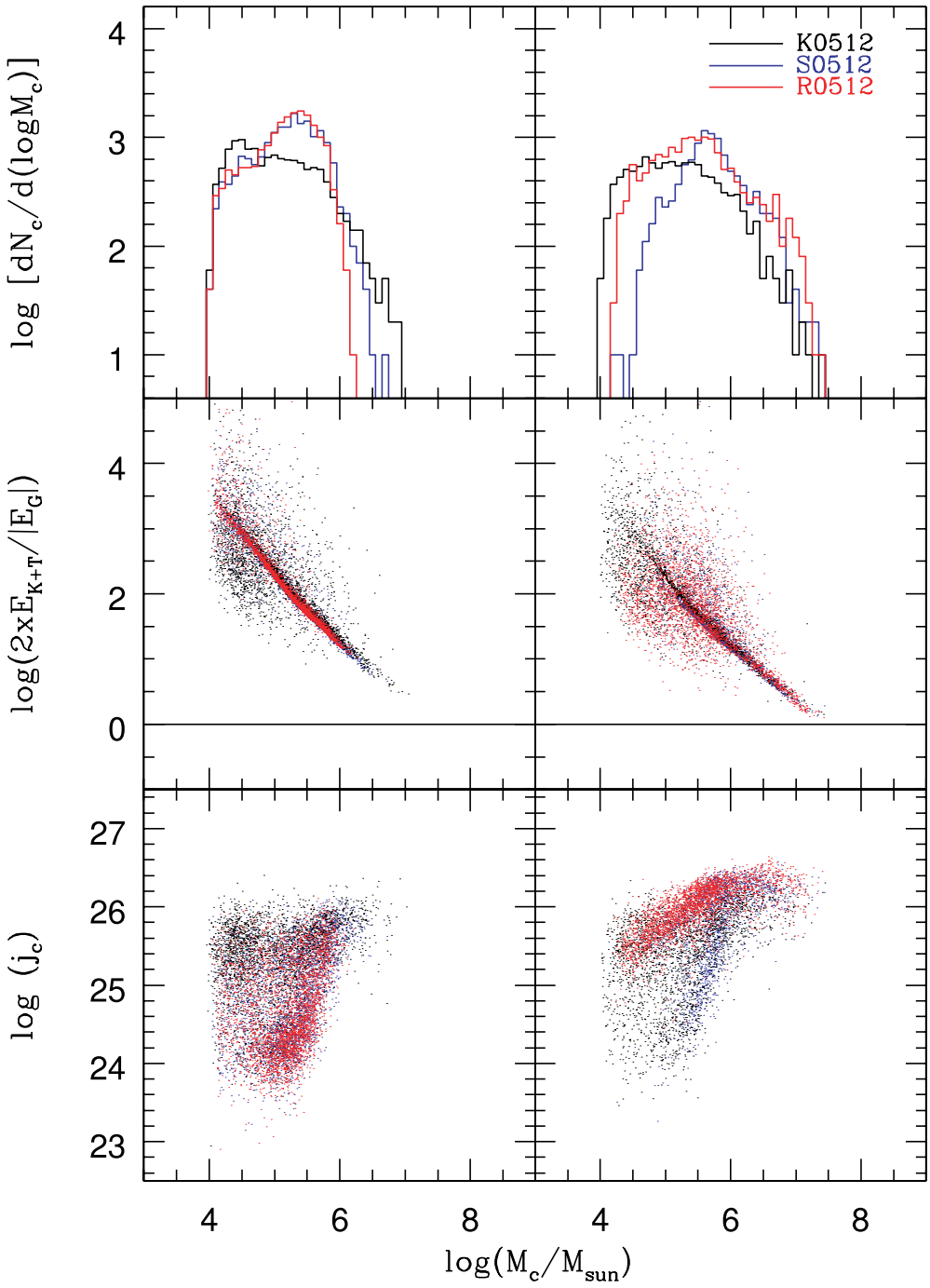

FIG. 12.—Differential number of clouds $dN_c/d(\log M_c)$, energy ratio $2(E_T + E_K)/|E_G|$, and specific angular momentum j_c as a function of cloud mass, M_c, in the three models with different initial density power spectra. The left panels are at $3t_{\rm cool}$, $6t_{\rm cool}$, and $11t_{\rm cool}$ for models K0512, S0512, and R0512, respectively. The right panels are at $4t_{\rm cool}$, $10t_{\rm cool}$, and $19t_{\rm cool}$ for models K0512, S0512, and R0512, respectively. Here j_c is in cgs units.

partly because the plotted time is different in different models. But the angular momentum of the clouds in the high-mass tail is similar. So we conclude that the properties of individual clouds, especially for massive clouds, are not sensitive to the initial perturbations, while the spatial distribution of clouds reflects the slope of the initial density power spectrum.

3.8. *Effects of Different Density and Cooling*

The effects of gas density on the formation and evolution of clouds were examined with model D0512, which has the background density 3 times larger than that of model S0512. Otherwise the two models are identical (see Table 1). With $t_{\rm cool}/t_{\rm grav} \propto n_h^{-1/2}$, the gravity is relatively less important in model D0512. Figure 13 compares the mass function, virial parameter, and specific angular momentum of clouds in model D0512 (*red lines and dots*) with those in model S0512 at an early stage of TI ($5t_{\rm cool}$) and at a late stage of merging ($15t_{\rm cool}$), respectively. In model D0512 there are more clouds with larger mass, reflecting the higher background density. Yet, the virial parameter is almost identical in the two models, indicating that the background density is not important in determining the energetics of individual clouds. As a matter of fact, we found that the properties

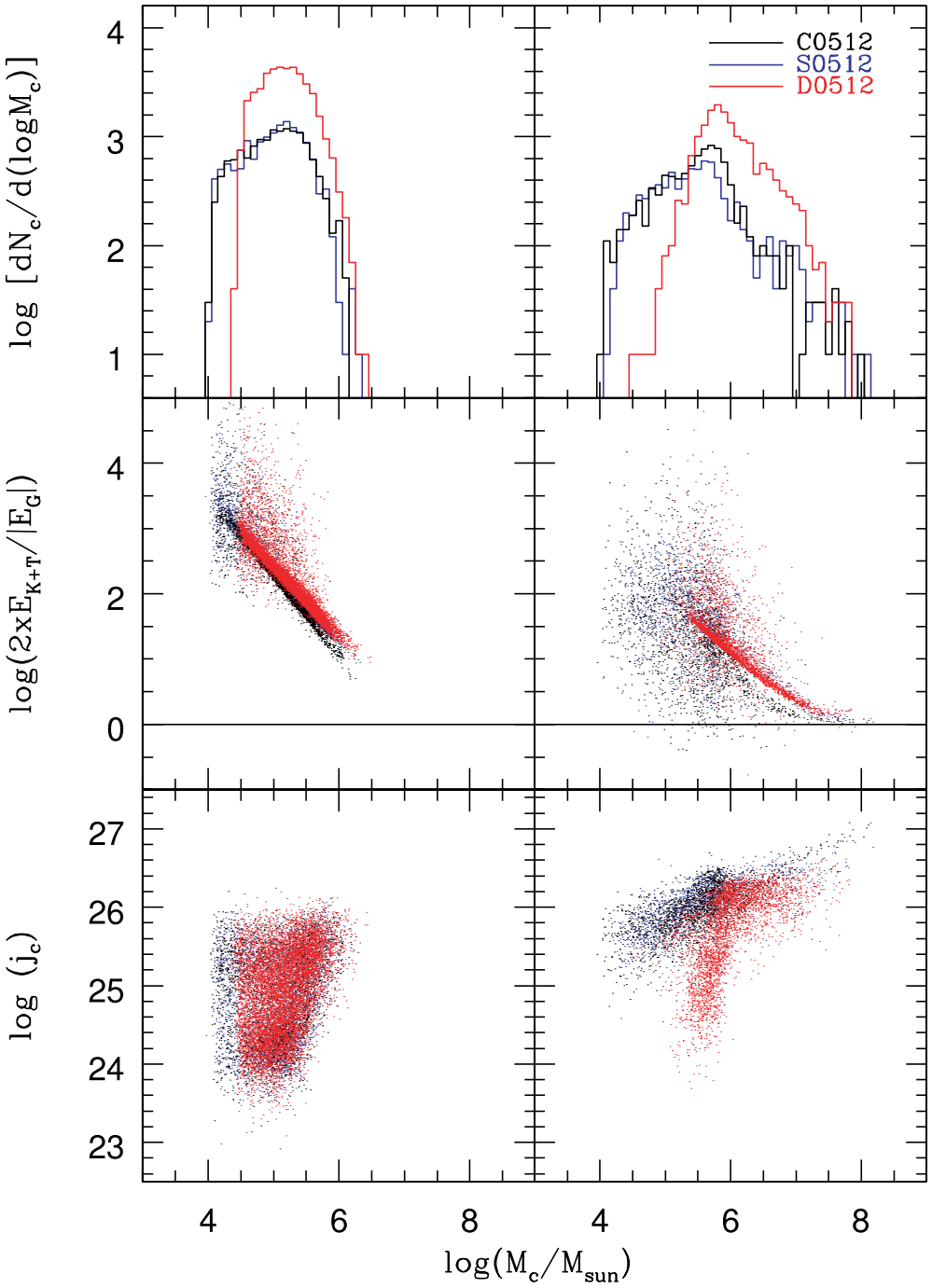

FIG. 13.—Differential number of clouds $dN_c/d(\log M_c)$, energy ratio $2(E_T + E_K)/|E_G|$, and specific angular momentum j_c as a function of cloud mass, M_c, in models C0512 and D0512, as well as in models S0512 for comparison. The left panels are at $5t_{\rm cool}$, and the right panels are at $15t_{\rm cool}$, respectively, for all three models. Here j_c is in cgs units.

of clouds, except the angular momentum, are not sensitive to the background density. The angular momentum of the clouds identified in the early stage of TI is similar in the two models. But in the late stage the angular momentum is noticeably smaller in the higher background density model. The same trend is also obvious in the spin parameter of gravitationally bound clouds, which is shown for $M_c \geq 10^7\ M_\odot$ in Figure 5. While the spin parameter for model S0512 (*blue triangles*) does not differ much from that for the higher resolution model S1024 (*red squares*), the spin parameter for model D0512 (*green circles*) is substantially smaller with the median value of $\lambda_{\rm med} \sim 0.12$. This is because the clouds formed in higher background density have experienced relatively less tidal torque and gravitational merging, through which they have acquired angular momentum.

The effects of possible further cooling to below 10^4 K were examined with model C0512, which includes the mock H_2 cooling given in equation (7). Otherwise it is same as model S0512 (see Table 1). Figure 13 compares the mass function, virial parameter, and specific angular momentum of clouds in model C0512 (*black lines and dots*) with those in model S0512. The

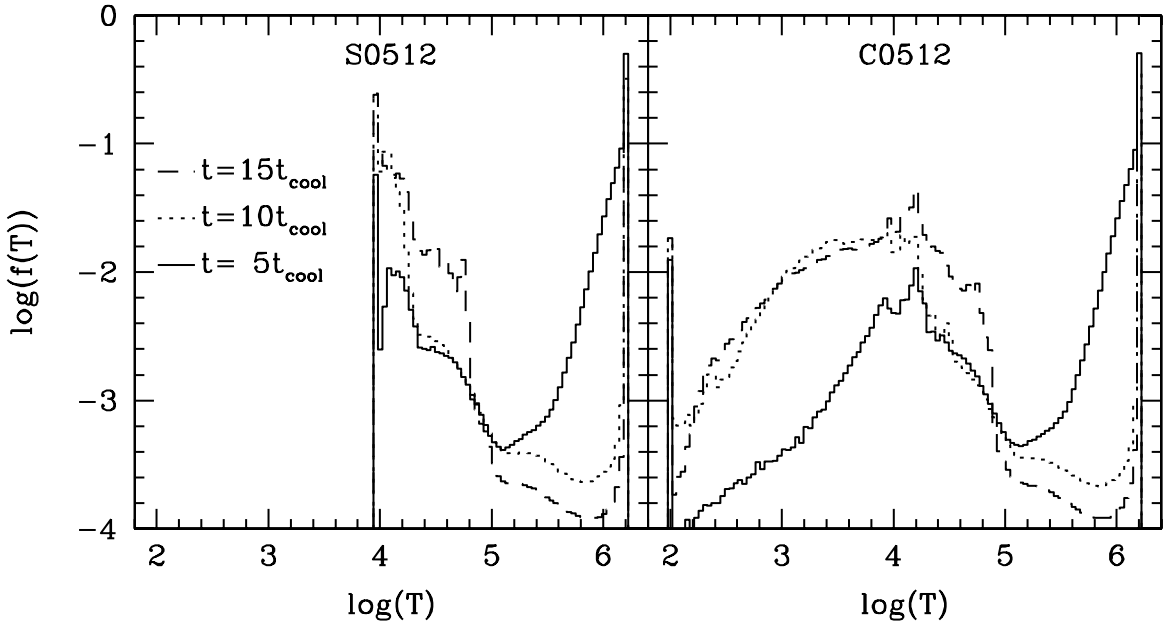

FIG. 14.—Mass fraction, $f(T)$, of gas as a function of temperature at three different times in models S0512 and C0512.

cloud properties are similar overall, except for the smaller thermal energy in model C0512, which is expected from the additional cooling. Because the thermal energy counts for most of the positive energy, especially in pressure-bound clouds, the virial parameter is smaller in model C0512. But in massive, gravitationally bound clouds, the kinetic energy is comparable to or sometimes larger than the thermal energy, as noted in § 3.3. So the effects of the additional cooling is less important in those clouds.

To quantify how much the additional cooling changes the thermal state of gas, we compare the mass distribution, $f(T)$, for models S0512 and C0512 in Figure 14. The gas with $T \sim 10^4$ K in S0512 spreads below 10^4 K in C0512, as expected. In addition, some of the gas with 10^4 K $\lesssim T \lesssim 2 \times 10^4$ K has cooled to below 10^4 K. But the additional cooling does not affect much the gas of higher temperature. Even with this additional cooling the mass fraction peaks still at $T \sim 1.5 \times 10^4$ K and most of the "cloud gas" has 10^3 K $\lesssim T \lesssim 10^5$ K, not only because the assumed mock H_2 cooling is inefficient, but also because some of the gas has been reheated by shocks and compression.

Here we should note that with lower temperature, the clouds in model C0512 have smaller Jeans mass and could go through further fragmentation. But with a fixed grid resolution, the simulation could not follow it. In fact, in model C0512, the Jeans number, $\Delta l/\lambda_J$, reached up to $\gtrsim 1$ in the center of some gravitationally bound clouds. However, as noted above, we did not intend to follow such fragmentation in this study.

4. SUMMARY AND DISCUSSION

We study the role of self-gravity and gravitational interactions in the formation of clouds via TI through three-dimensional hydrodynamic simulations. We considered the gas in the protogalactic halo environment with $T \sim 1.7 \times 10^6$ K and $n \sim 0.1$ cm^{-3} in a periodic box of 10 kpc and followed its evolution for up to 20 cooling times. We adopted idealized models in which a static, nonmagnetized gas cools radiatively with initial isothermal density perturbations. A radiative cooling rate in ionization equilibrium for an optically thin gas with the primordial composition was used. In addition, ad hoc heating was included, which emulates feedback from stellar winds, supernovae, turbulence, and shocks in order to maintain the thermal balance of background gas.

The main results can be summarized as follows. (1) Clouds form first on scales much smaller than the cooling length as a result of the nonlinear behavior of TI. (2) Those small clouds grow through compression by background pressure, as well as through gravitational infall, but eventually they merge by gravity and become gravitationally bound objects. (3) The gravitationally bound clouds acquire angular momentum through merging, as well as tidal torque. So they have high angular momentum with a spin parameter of $\langle \lambda_s \rangle \sim 0.3$ or so. (4) The spatial distribution of clouds depends on initial perturbations, for instance the slope of the initial density power spectrum, but the properties of individual clouds are not sensitive to that.

We note that a realistic picture of thermal-gravitational instability in protogalactic halos would be more complex than in the numerical models considered here. Some of the key aspects include the following: (1) The gas in real protogalactic halos is likely in a chaotic state induced during the formation of the halos themselves. The chaotic flow motions would have suppressed the early formation of clouds via TI but increased collisions of clouds once formed. (2) Protogalactic halos have their own structures, but the effects of those structures were ignored. For instance, the tidal torque exerted by the halo and/or the rotation in a disk would have suppressed the formation of clouds. (3) There are emerging evidences that magnetic fields existed even in the early galaxies where the oldest stars formed (see, e.g., Zweibel 2003). Then, undoubtedly the magnetic field would have affected the formation and properties of clouds profoundly. (4) It is well known that when a hot gas cools from $T > 10^6$ K, it recombines out of ionization equilibrium because the cooling timescale is shorter than the recombination timescale (Shapiro & Kang 1987). However, details of the cooling, such as nonequilibrium ionization and H_2 and metal cooling to below 10^4 K, could have only minor effects on our main conclusions.

Although the numerical models are rather idealized to facilitate simulations, our results should provide crude insights on the formation of PGCCs in protogalactic halos. The gravitationally

bound clouds in our simulations have mass $M_c \gtrsim 10^7\ M_\odot$ and radius $R_c \simeq 150$–200 pc. If some of them had evolved into PGCCs and became globular clusters, they should have lost $\sim$90% of their mass with $\sim$10% of star formation efficiency, and at the same time they should have collapsed by a factor 10 or so. But the further collapse would not have been straightforward because of large angular momentum, unless their angular momentum was removed very efficiently along with mass during the star formation phase. Such removal of angular momentum may not be impossible, but following it is beyond the scope of this numerical study. It should be studied with simulations that have resolution high enough to follow the fragmentation of clouds and the subsequent formation of stars inside PGCCs. However, we make the following note of caution. The clouds in our simulations continue to grow mostly through merging in the late stage, and thus their mass and angular momentum increase over time. So any simulations of isolated clouds to study the ensuing evolution of PGCCs could be misleading.

We should point out that there is a caveat in our argument for the large angular momentum of gravitationally bound clouds. The angular momentum was acquired mostly through gravitational processes, i.e., tidal torque and merging. So if the clouds formed in an environment where the gravitational processes are less important, they would have acquired less angular momentum. For instance, we showed that the clouds formed in a denser background have smaller angular momentum. Hence, if protogalactic halos consisted of smaller halolets and clouds formed in shocked regions after the collisions of halolets, as suggested by, e.g., Gunn (1980), they could have smaller angular momentum.

We thank the anonymous referee for constructive comments. The work of C. H. B., H. K., and J. K. was supported by KOSEF through the Astrophysical Research Center for the Structure and Evolution of Cosmos (ARCSEC). The work of D. R. was supported by a Korea Research Foundation grant (KRF-2004-015-C00213). Numerical simulations were performed using the Linux Cluster for Astronomical Calculation of KASI-ARCSEC.

APPENDIX

CORRECTED POTENTIAL

In our simulations, the gravitational potential for the gasdynamical equation in § 2.2 was calculated by using the FFT method, $\Phi_{\rm FFT}(\boldsymbol{r})$. Then the gravitational force could be correctly calculated by differentiating this potential on a grid. However, the use of $\Phi_{\rm FFT}(\boldsymbol{r})$ to calculate the gravitational energy of clouds, E_G, in § 3.3 results in a large error, because $\Phi_{\rm FFT}(\boldsymbol{r})$ is undetermined by an integral constant. In principle, the gravitational potential of isolated clouds can be precisely calculated by the direct double integration over cloud volume. However, the computational cost of this method is prohibitively expensive, especially for gravitationally bound clouds in the 1024^3 simulation, since they occupy typically $\sim 10^4$ or so grid zones. One the other hand, direct integration does not take account of the contributions from the rest of mass in the simulation box as well as the periodic mass distribution. But we found that those contributions are small, especially for massive, gravitationally bound clouds.

In an effort to estimate the gravitational energy of clouds more accurately, we devised a method that calculates and uses the corrected potential as follows:

1. The position, $\boldsymbol{r}_{\rm min}$, at which $\Phi_{\rm FFT}(\boldsymbol{r})$ has the minimum value is found for each cloud, and then the potential at the position is calculated by direct integration:

$$\Phi_{\rm direct}(\boldsymbol{r}_{\rm min}) = -G \int \frac{\rho(\boldsymbol{r}')}{|\boldsymbol{r}' - \boldsymbol{r}_{\rm min}|}\, dV'. \tag{A1}$$

2. The difference between $\Phi_{\rm direct}$ and $\Phi_{\rm FFT}$ at $\boldsymbol{r}_{\rm min}$ is calculated for each cloud:

$$C = \Phi_{\rm direct}(\boldsymbol{r}_{\rm min}) - \Phi_{\rm FFT}(\boldsymbol{r}_{\rm min}). \tag{A2}$$

3. Then the corrected potential for each cloud is calculated by

$$\Phi_{\rm corr}(\boldsymbol{r}) = \Phi_{\rm FFT}(\boldsymbol{r}) + C. \tag{A3}$$

4. Finally, the gravitation energy of each cloud is calculated as

$$E_G = \int \frac{1}{2}\rho(\boldsymbol{r})\Phi_{\rm corr}(\boldsymbol{r})\, dV. \tag{A4}$$

Figure 15 demonstrates the motivation of our effort. Here E_{N^2} is the gravitational energy of clouds calculated by direct double integration, while $E_{\rm FFT}$ and $E_{\rm corr}$ were calculated using $\Phi_{\rm FFT}$ and $\Phi_{\rm corr}$, respectively. The errors for model S0256 are shown when the double integration could be done with a reasonable computation time. $E_{\rm corr}$ tends to agree with E_{N^2} better than $E_{\rm FFT}$. With $E_{\rm corr}$ the error is within $\sim$20% or so for a substantial fraction of clouds. However, the estimation of gravitational energy could easily be off by a factor of 2 or even larger with $E_{\rm FFT}$. We used $E_{\rm corr}$ for the gravitational energy in § 3.3.

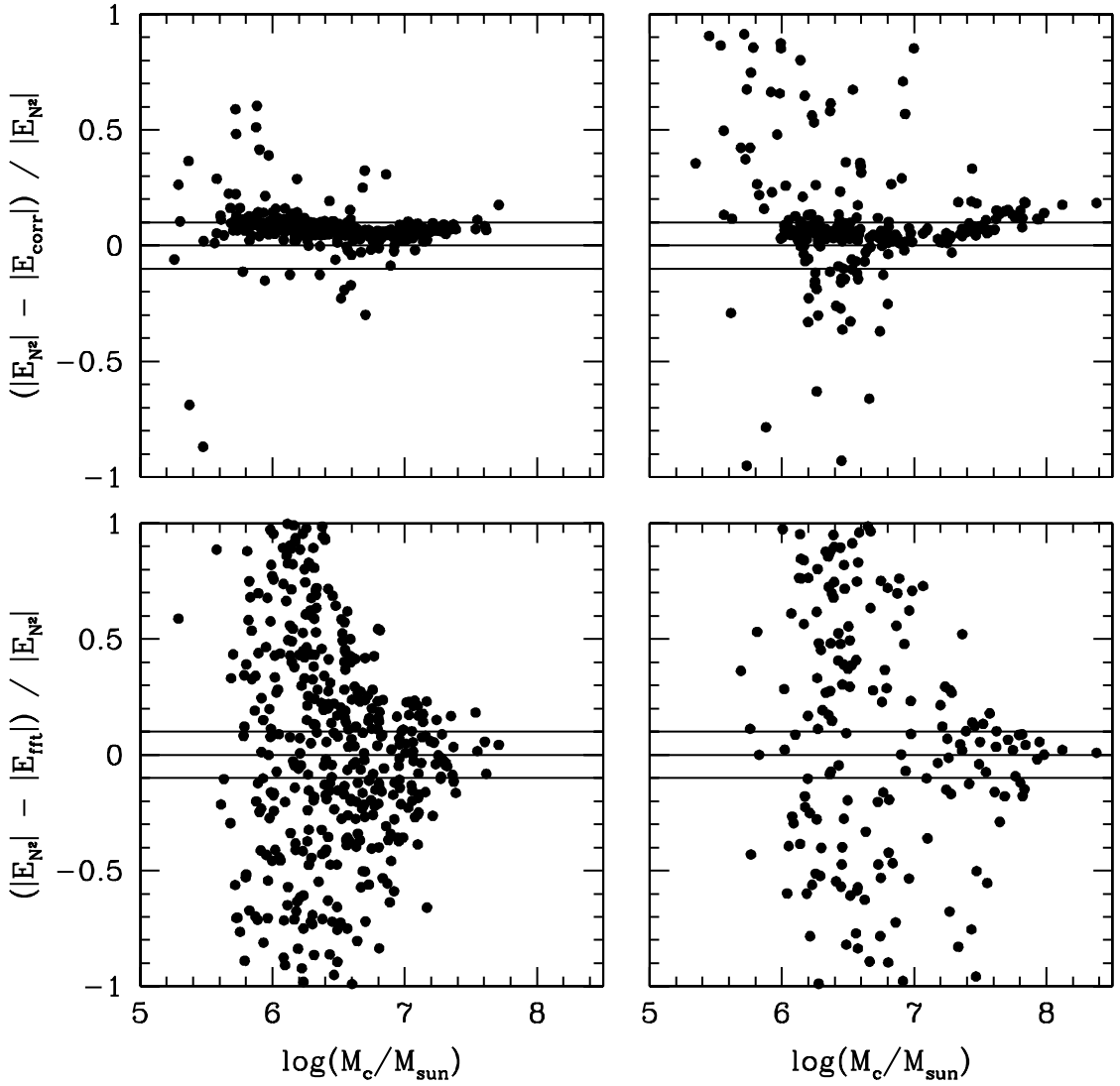

FIG. 15.—Error in the estimation of gravitational energy by the FFT potential (*bottom panels*) and the corrected potential (*top panels*) at $10t_{\rm cool}$ (*left panels*) and $15t_{\rm cool}$ (*right panels*) in model S0256. See the Appendix for details.

REFERENCES

Baek, C. H., Kang, H., & Ryu, D. 2003, ApJ, 584, 675
Balbus, S. A. 1986, ApJ, 303, L79
Barnes, J., & Efstathiou, G. 1987, ApJ, 319, 575
Brinkman, W., Massaglia, S., & Müller, E. 1990, A&A, 237, 536
Burkert, A., & Lin, D. N. C. 2000, ApJ, 537, 270
Chandran, B. D. G., & Cowley, S. C. 1998, Phys. Rev. Lett., 80, 3077
Curir, A., Diaferio, A., & de Felice, F. 1993, ApJ, 413, 70
David, L. P., Bregman, J. N., & Seab, C. G. 1988, ApJ, 329, 66
Fall, S. M., & Rees, J. M. 1985, ApJ, 298, 18
Field, G. B. 1965, ApJ, 142, 531
Field, G. B., Goldsmith, D. W., & Habing, H. J. 1969, ApJ, 155, L149
Gammie, C. F., & Lin, Y. T. 2003, ApJ, 592, 203
Gunn, J. E. 1980, in Globular Clusters, ed. D. Hanes & G. Madore (Cambridge: Cambridge Univ. Press), 301
Kang, H., Lake, G., & Ryu, D. 2000, J. Korean Astrophys. Soc., 33, 111
Koyama, H., & Inutsuka, S. 2002, ApJ, 564, L97
———. 2004, ApJ, 602, L25
Kravtsov, A. V., & Gnedin, O. Y. 2005, ApJ, 623, 650
Kritsuk, A. G., & Norman, M. L. 2002, ApJ, 569, L127
Malagoli, A., Rosner, R., & Fryxell, B. 1990, MNRAS, 247, 367
McCrea, W. H. 1957, MNRAS, 117, 562
McKee, C. F., & Begelman, M. C. 1990, ApJ, 358, 392
McKee, C. F., & Ostriker, J. P. 1977, ApJ, 218, 148
Nulsen, P. E. J. 1986, MNRAS, 221, 377
Parmentier, G., Jehin, E., Magain, P., Neuforge, C., Noels, A., & Thoul, A. A. 1999, A&A, 352, 138
Peebles, P. J. E. 1969, ApJ, 155, 393
Ryu, D., Ostriker, J. P., Kang, H., & Cen, R. 1993, ApJ, 414, 1
Shapiro, P. R., & Kang, H. 1987, ApJ, 318, 32
Shustov, B. M., & Wiebe, D. S. 2000, MNRAS, 319, 1047
Spitzer, L., Jr. 1979, Physical Processes in the Interstellar Medium (New York: Wiley)
Sutherland, R, S., & Dopita, M. A. 1993, ApJS, 88, 253
Truelove, J. K., Klein, R. I., McKee, C. F., Holliman, J. H., II, Howell, L. H., & Greenough, J. A. 1997, ApJ, 489, L197
Vázquez-Semadeni, E. 1994, ApJ, 423, 681
Wada, K., & Norman, C. A. 2001, ApJ, 547, 172
Williams, J. P., De Geus, E. J., & Blitz, L. 1994, ApJ, 428, 693
Zweibel, E. G. 2003, ApJ, 587, 625